Optimization of the Guiding Stability of a Horizontal Axis HTS ZFC Radial Levitation Bearing

António J. Arsénio, F. Ferreira da Silva, João F. P. Fernandes, and P. J. Costa Branco

[1] Instituto de Engenharia Mecânica (IDMEC), Instituto Superior Técnico (IST), Universidade de Lisboa, Portugal

antoniojcosta@tecnico.ulisboa.pt, pbranco@tecnico.ulisboa.pt

Abstract

This document presents a study on the optimization of the 3D geometry of a horizontal axis radial levitation superconducting magnetic bearing with zero-field cooled (ZFC) high-temperature superconductor (HTS) bulks in the stator and radially magnetized permanent magnet (PM) rings in the rotor. A previous study on optimizing the 3D geometry for minimization of volume or cost considering variable dimensions of components and variable spacing was done. This initial optimization concerned only the maximization of the levitation force with a given restriction for the minimum levitation force.

Although the used geometry promotes the creation of guidance with ZFC, guiding forces depend on the spacings between PM rings in the rotor and between the rings of HTS bulks in the stator. This new optimization study aims to find the optimum spacings that maximize the guiding force for specific HTS bulk and PM ring dimensions while maintaining the minimum required levitation force. All the optimizations are based on using the non-dominated sorting genetic algorithm (NSGA-II) over 3D finite element analysis (FEA). A simplified electromagnetic model of equivalent relative permeability, calibrated with experimental measurement of magnetic levitation forces, is used on 3D FEA to reduce significantly numerical processing and optimization time.

Specifically optimized geometries for the experimental prototype were tested to validate optimization results. The experimental prototype is made of a stator of high-density polyurethane walls containing chambers where yttrium boron copper oxide (YBCO) bulks are immersed in liquid nitrogen (LN2). To hold the neodymium iron boron (NdFeB) PM rings, the rotor structure is made of polylactic acid plastic printed by a 3D computer numeric control (CNC) printer. An analysis of stable and unstable geometries domains depending on the spacings between HTS rings and PM rings is also done for two HTS bulk sizes.

1 Introduction

The studied horizontal axis radial levitation high-temperature superconductor (HTS) magnetic bearing comprises a stator with two cryostat chambers housing two discontinuous rings of zero-field cooled HTS bulks and a permanent magnet (PM) rotor with three radially magnetized PM rings with alternating polarization. Each HTS ring is positioned in the zone between adjacent PM rings.

With a uniform distribution of HTS bulks around the stator chambers, the obtained levitation force is zero with no vertical deviation of the rotor. Due to its weight, it is not possible to keep the rotor levitating at the center position. To maximize the available net force (difference between levitation force and the rotor weight), making possible the experimental measurement of levitation forces to validate electromagnetic model parameters, a topology with only 6 HTSs on the bottom of the stator was considered in experimental measurements. Figure 1(a) shows a geometry of the studied bearing, Figure 1(b) an exploded 3D view of the experimental prototype design, and Figure 1(c) a 3D perspective of its assembly.

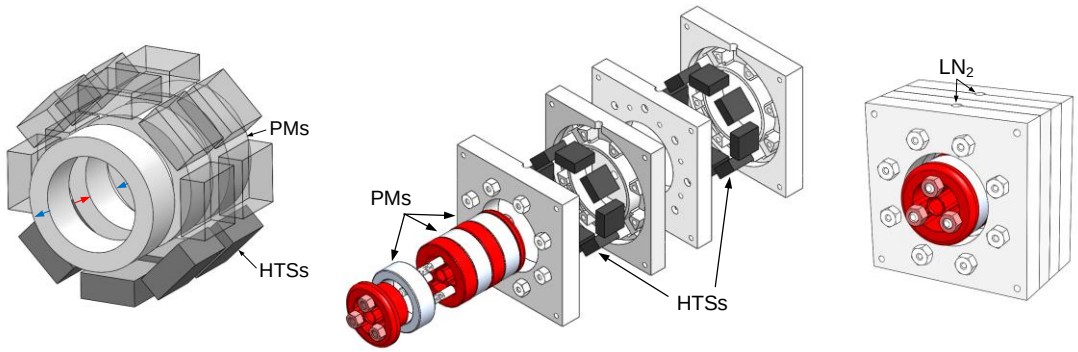

Figure 1: (a) Geometry of the studied bearing, (b) 3D exploded view design, and (c) assembly design of the experimental prototype.

In the experimental prototypes built and tested, the stator has two chambers of rigid high-density polyurethane walls, each one housing one discontinuous ring of HTS bulks. The stator walls were built by a computer numeric control (CNC) milling machine. The rotor structure in polylactic acid plastic (PLA) was printed by a 3D computer-aided design (CAD) printer (Arsénio, A.J., 2016).

Initially, a first stator named Stator I, for housing $33 \times 33 \times 14$ mm^3 size bulks was built. This stator and two rotors with 5 mm and 20mm spacings between PM rings, named respectively as rotors D5 and D20, were used to measure magnetic levitation and guidance forces and validate electromagnetic model parameters (Arsénio, A.J., 2018). Studies on the LN_2 consumption and YBCO bulk temperature evolution for different thermal processes in the initial ZFC and operation of the experimental bearing prototype were presented in (Arsénio, A.J., 2018) and (Arsénio, A.J., 2021). Work on optimizing the superconducting linear magnetic bearing of a maglev vehicle was presented (Quéval, L., 2016). A study on multi-objective multi-constraint optimization of the 3D geometry to minimize the bearing cost or volume was also performed (Fernandes, J.F.P, 2020). Optimizations using the non-dominated sorting genetic decision algorithm NSGA-II over 3D finite element analysis (FEA) were applied to obtain the optimized levitation forces. An equivalent relative permeability model was adopted for the 3D FEA to reduce the time consumption on the numerical processing significantly. This initial optimization study was based on maximizing levitation forces, not looking to guarantee and maximize the guiding stability. The optimizations are considered a restriction to guarantee a minimum levitation force equal to the one obtained with the geometry defined by 6 HTS bulks at the bottom of Stator I and

rotor D5. Figure 2 compares this restriction geometry with the resulting cost and volume optimized geometries.

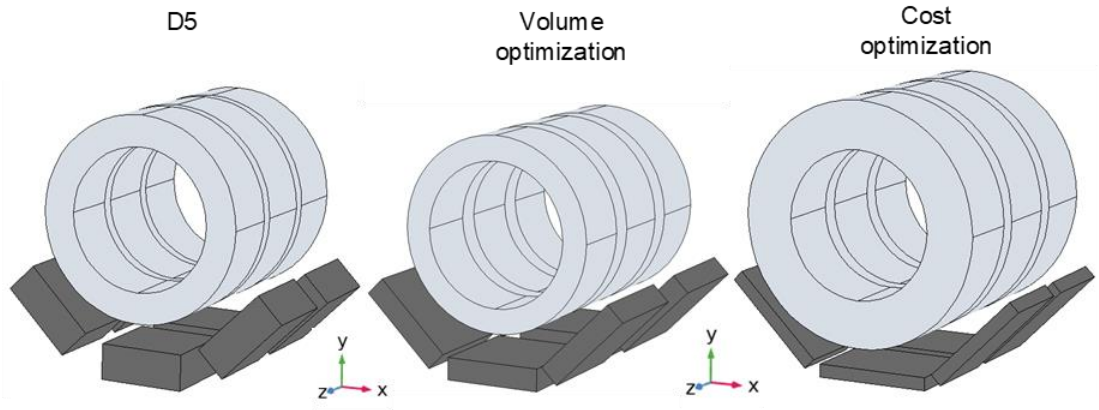

Figure 2: (a) Geometry with rotor D5 and 6 HTS bulks of $\mathbf{33 \times 33 \times 14\ mm^3}$, (b) Volume, and (c) Cost optimized geometries.

Another stator named Stator II for housing bulks with dimensions $40 \times 40 \times 10\ \mathrm{mm}^3$, close to the bulk dimensions in the volume optimized geometry was built. Figure 3 shows the chamber profiles of Stator I and Stator II.

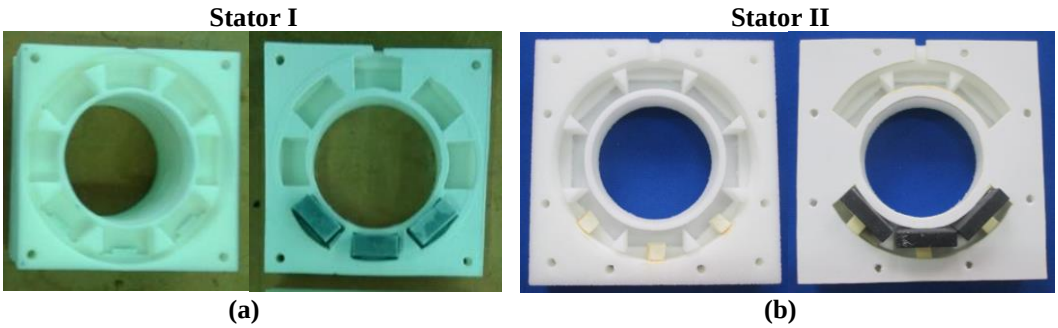

Figure 3: Chamber profiles of (a) Stator I for $33 \times 33 \times 14\ \mathrm{mm}^3$ size bulks, and (b) Stator II for $40 \times 40 \times 10\ \mathrm{mm}^3$ size bulks.

This document presents a study on optimizing the spacings between HTS bulk rings in the stator and between PM rings in the rotor, to maximize the guiding force and so the guiding stability with a restriction on the minimum levitation force that should be guaranteed. Also, the determination of the domains in which the combination of rotor PM rings spacings and stator HTS ring spacings guarantee guiding stability is performed. This is done for the two bulk-size stators.

The purpose of using ZFC is to minimize the magnetization energy and Joule losses in the bulks, increasing their lifetime with the benefit of increasing levitation forces. Because with ZFC, there is no flux pinning as with FC, guiding stability is guaranteed by geometries with a specific arrangement of PMs and spatial distribution of HTSs. Thus, it is of extreme importance to determine which geometries present some guiding stability and find the optimum spacings between HTS rings and between PM rings to maximize the guiding stability for a given restriction on the minimum levitation force be guaranteed.

2 Electromagnetic models and parameters

The E-J model described below should be used for a detailed prediction and characterization of the induced current distribution in HTS bulks. This model implies the resolution of non-linear and partial differential equations in the superconductor domain, requiring a lot of numerical processing in the FEA. A simplified model with a calibrated value of equivalent relative permeability was used to significantly reduce the FEA processing time, especially during the optimization of the bearing 3D geometry.

2.1 E-J model

When after ZFC, a magnetic field $\mathbf{H_a}$ is applied to a superconductor bulk, an electric field **E** is induced from the variation of the penetrating magnetic field **H**, according to Faraday's law.

$$\boldsymbol{\nabla} \times \mathbf{E} = -\mu_0 \frac{\mathrm{d}\mathbf{H}}{\mathrm{dt}} \tag{1}$$

According to the model in (Hong. Z., 2007), type II superconductors present a non-linear electric conductivity characteristic given by the power-law (2),

$$E = E_0 \left(\frac{J}{J_c}\right)^n \tag{2}$$

where E and J are the magnitudes respectively of induced electric field and current density, J_c the critical current density and E_0 is the electrical field at which the current density reaches J_c. Exponent n is a positive integer higher than 1. The induced current density **J** creates, by Ampere's law, a magnetization field **M**.

$$\mathbf{J} = \nabla \times \mathbf{M} \tag{3}$$

The penetrating magnetic field is given by the sum of the applied magnetic field and the magnetization field.

$$\mathbf{H} = \mathbf{H_a} + \mathbf{M} \tag{4}$$

According to the Kim-Anderson model in (Yamamoto, K., 1993) and (Fujishiro, H., 2010), the critical-current density J_c depends on the absolute value of the penetrating magnetic-flux density $|B|$,

$$J_c(B) = J_{c0} \frac{B_0}{B_0 + |B|} \tag{5}$$

where J_{c0} is the zero-field critical current density that depends on the temperature T (Koo, J., 2004), and B_0 the magnitude of the penetrating magnetic flux density for which the critical current density is half the zero-field critical current density. For the case of yttrium barium copper oxide (YBCO), $E_0 = 1 \times 10^{-4}\ \mathrm{Vm}^{-1}$, $B_0 = 0.1\ \mathrm{T}$ and $n = 21$ (Zhang, M, 2012). Appropriate values of the parameter J_{c0} can be validated by comparing the magnetic forces predicted by FEA using the E-J model with the ones obtained by experimental measurement.

2.2 Equivalent relative permeability model

The relative permeability μ_r is defined by the relation between the magnitude of the penetrating field H and the magnitude of the applied magnetic field H_a, being calculated by (6).

$$\mu_r = \frac{H}{H_a} = 1 + \frac{M}{H_a} = 1 + \chi \tag{6}$$

where χ is the magnetic susceptibility. Perfect diamagnetism is traduced by χ equal to -1 and μ_r equal to 0.

In this model, an average value of relative permeability $\overline{\mu_r}$ designated by the equivalent relative permeability is considered. A methodology to compute the value of $\overline{\mu_r}$ for the total bulk volume was initially proposed in (Arsénio, A. J., 2016) and (Fernandes, J.F.P, 2020). Based on the first methodology, a more generic methodology to compute values of $\overline{\mu_r}$ in several partitions of the bulk was then proposed in (Inês, P., 2021).

Appropriate values of $\overline{\mu_r}$ can be validated by comparing the magnetic forces predicted by FEA with the ones obtained by experimental measurement. The use of this model significantly reduces the FEA numerical processing.

3 Validation of electromagnetic model parameters

Magnetic levitation and guidance forces were measured experimentally and determined by 3D FEA for two geometries respectively with rotors D20 and D5 and with 6 YBCO bulks of volume $33 \times 33 \times 14$ mm^3 on the bottom of Stator I. In these two geometries, the spacing between the two YBCO bulk rings was 10 mm. Figures 4(a) and 4(b) show the dimensioned 3D perspective design (half part used in FEA simulations) of these two geometries tested experimentally.

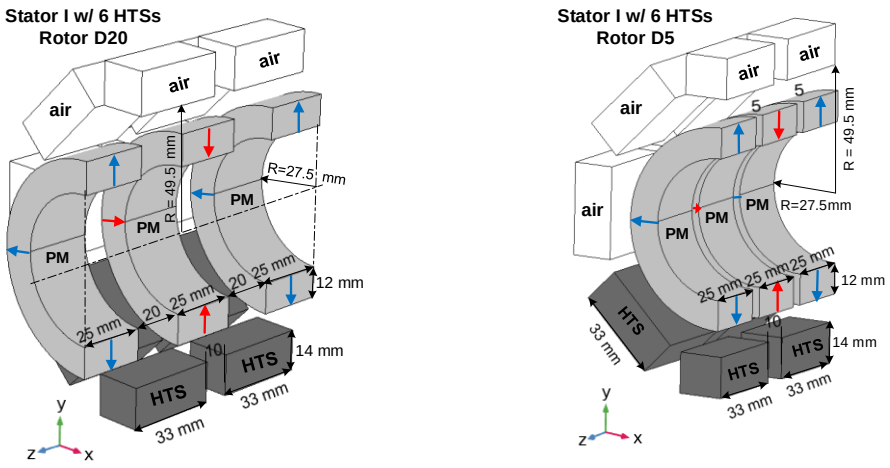

(a) **(b)**

Figure 4: Dimensioned 3D perspective of the half part (used in FEA simulations) of the tested geometries with 6 HTS bulks on the bottom of stator I and with (a) rotor D20 and (b) rotor D5.

Figures 5(a) and 5(b) show respectively transversal and longitudinal views of the magnetic flux and current density distributions for the geometry with rotor D20. Figures 6(a) and 6(b) refer to the geometry with rotor D5. The results were obtained using the *E-J* model with $J_{c0} = 8 \times 10^7$ Am^{-2}.

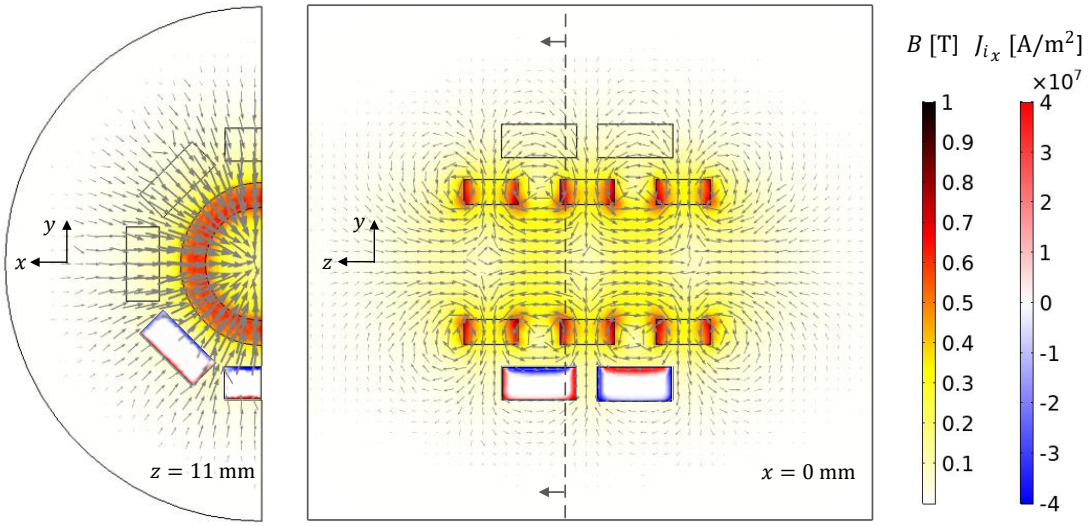

Figure 5: (a) Transversal and (b) longitudinal views of the magnetic flux and current density distributions for the geometry with 6 HTSs bulks on the bottom of Stator I and rotor D20.

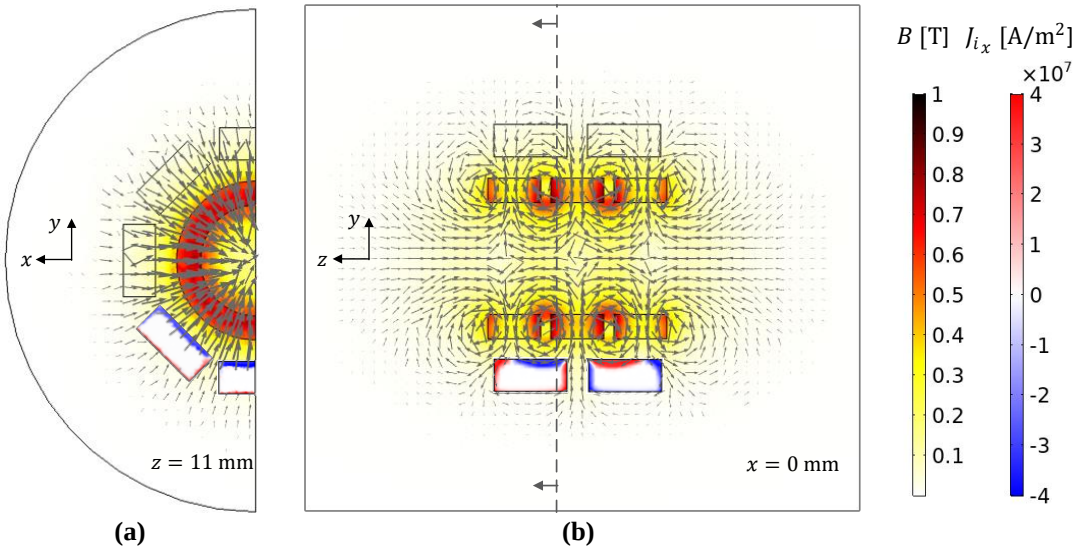

Figure 6: (a) Transversal and (b) longitudinal views of the magnetic flux and current density distributions for the geometry with 6 HTSs bulks on the bottom of Stator I and rotor D5.

Experimental measurements and FEA simulations were performed to verify the dependence of the levitation force with the rotor vertical deviation and the dependence of the guidance force with the rotor axial deviation keeping the rotor axis on the central position.

Figures 7(a) and 7(b) show pictures respectively of rotors D20 and D5, indicating the gravity force F_g of their weights. Figure 7(c) shows a photo of Stator I, with a fixed spacing of 10 mm between the two rings of HTS bulks. Figures 7(d) e 7(e) show the setups to measure the levitation force with the vertical deviation and the guidance force with the axial deviation.

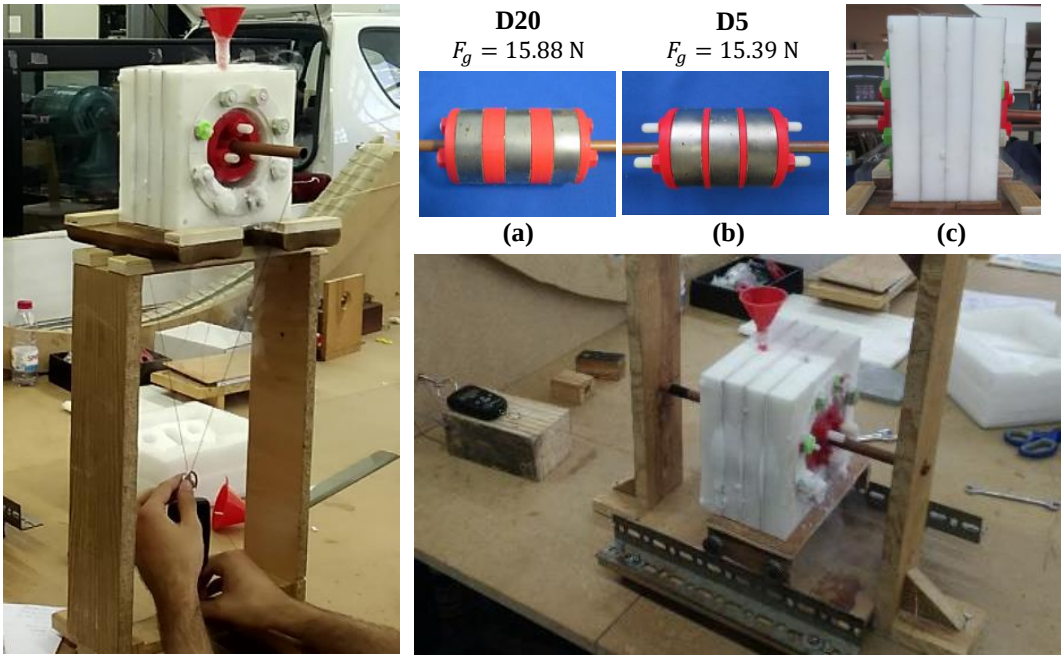

Figure 7: (a) Rotor D20, (b) Rotor D5, (c) Stator I with a spacing of 10 mm between HTS rings, and experimental setups to measure (d) levitation and (e) guidance forces.

The characteristics of dependence of the levitation force with the vertical displacement obtained by FEA using the equivalent permeability model and the E-J model and by experimental measurement respectively with Rotor D20 and Rotor D5 are shown in Figures 8(a) and 8(b). For each rotor deviation, 3D FEA simulations were performed between 1.5 hour and 6 hours with the *E-J* model and less than 30 s with the equivalent permeability model.

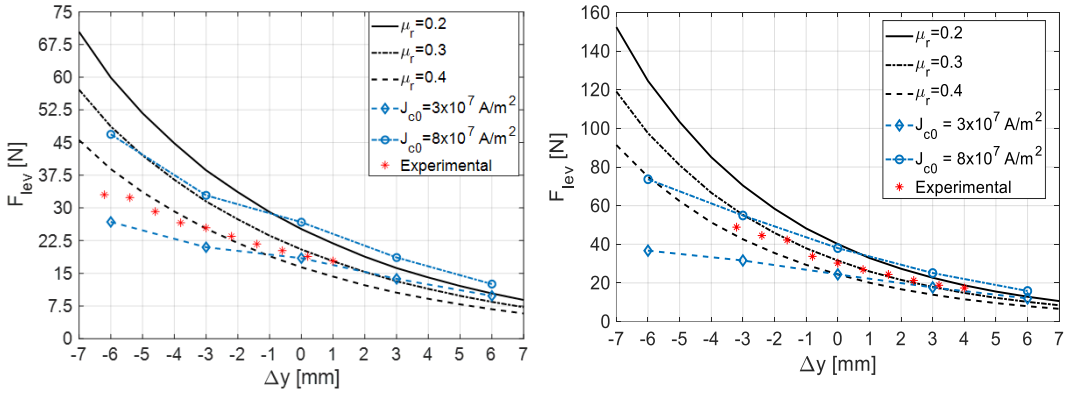

Figure 8: Dependence of the levitation force with vertical displacement by FEA using the equivalent permeability model and the E-J model and experimentally with (a) Rotor D20 and (b) Rotor D5.

As one may verify, the experimental values follow the monotony of the characteristics with the *E-J* model between $J_{c0} = 3 \times 10^7$ Am^{-2} and $J_{c0} = 8 \times 10^7$ Am^{-2}. For the second case with rotor D5, these are closer to the characteristic with $J_{c0} = 8 \times 10^7$ Am^{-2}. With Rotor D5 in the center position (no

vertical deviation), the levitation force with $J_{c0} = 8 \times 10^7$ Am^{-2} is between the ones predicted with $\overline{\mu_r} = 0.2$ and $\overline{\mu_r} = 0.3$, close to the one that would be predicted with $\overline{\mu_r} = 0.25$. For a lower distance g_a between the HTSs to the PMs, the higher is the value of equivalent relative permeability for which the predicted levitation forces approximates experimental values. This is because the closer the PMs are to the HTSs, the higher the penetrating field.

Figures 9(a) and 9(b) show the characteristics of dependence of the levitation force with the vertical displacement obtained by FEA using the equivalent permeability model and the *E-J* model and experimental measurement, respectively with Rotor D20 and Rotor D5.

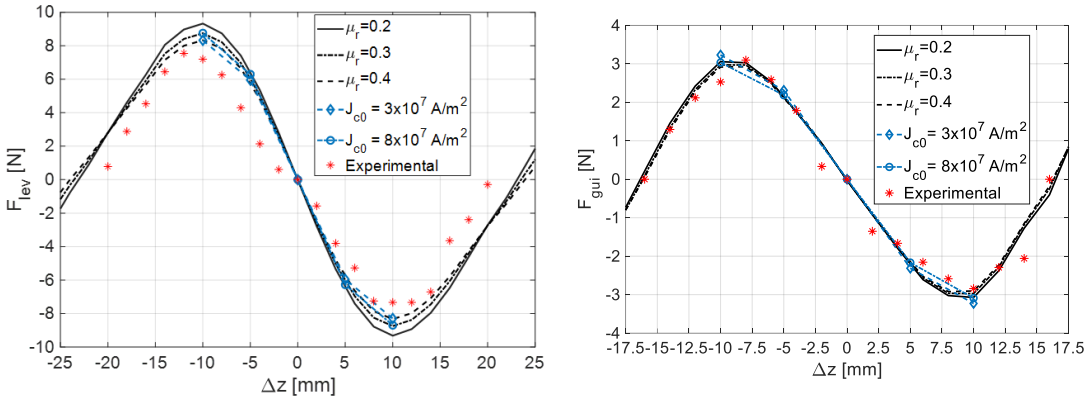

(a) **(b)**

Figure 9: Dependence of the guidance force with axial displacement by FEA using the equivalent permeability model and the E-J model and experimentally with (a) Rotor D20 and (b) Rotor D5.

As one may verify, the sensitivity of the guidance force to the value of $\overline{\mu_r}$ is much less than the one verified for the case of the levitation force. With the rotor at the center position, the applied magnetic field did not change notably in the range of axial deviations applied.

Table I resumes the values of levitation force F_{lev} with the rotor at the center position, predicted by FEA and obtained by experimental measurement. The last column presents the net force F_n (difference between levitation force F_{lev} and the gravity force F_g of the rotor weight) relatively to the experimental measurement.

Table I: Experimental and FEA values of F_{lev} with Rotor D20 and D5 at the center position.

$\Delta x = \Delta_y = 0$ mm $\Delta z = 0$ mm	F_{lev} [N]							F_n [N] Exp.
	$\mu_r =$ 0.2	$\mu_r =$ 0.25	$\mu_r =$ 0.3	$\mu_r =$ 0.4	$J_{c0} =$ 3×10^7 Am^{-2}	$J_{c0} =$ 8×10^7 Am^{-2}	Exp.	
Rotor D20 $F_g = 15.88$ N $g_a = 10.5$ mm	25.15	22.72	**20.47**	16.40	**18.47**	23.73	**19.19**	3.31
Rotor D5 $F_g = 15.39$ N $g_a = 10.5$ mm	37.62	**31.39**	26.17	21.44	22.42	**32.31**	**30.26**	14.87

With the rotors at the center position, the levitation force predicted with $J_{c0} = 8 \times 10^7$ Am^{-2} is close to the one predicted with $\overline{\mu_r} = 0.25$. The experimental are between the ones with $J_{c0} = 3 \times 10^7$ Am^{-2} and $J_{c0} = 8 \times 10^7$ Am^{-2}, being closer to the one with $J_{c0} = 8 \times 10^7$ Am^{-2} on the case of Rotor D5. With

a stator made of a material with better thermal insulation than the used polyurethane foams, the average temperature of bulks would decrease, and levitation forces would get closer to the ones predicted using the *E-J* model with $J_{c0} = 8 \times 10^7$ Am^{-2}.

4 Optimization of the HTS and PM ring spacings to maximize the guiding stability

A previous study to optimize the volume and cost of the 3D geometry with a given constrain on the minimum net levitation force was performed. Optimizations were performed using the non-dominated sorting genetic algorithm NSGA-II over 3D FEA results. In this first study, the component dimensions and spacings were all considered as decision variables. The dimensions of the bulks used in Stator II are close to the ones indicated by the volume optimization.

This study aims to optimize the spacing between the two rings of HTS bulks in the stator and the spacings between PM rings in the rotor for given bulk and PM ring sizes, maintaining the minimum required levitation forces. Bulk sizes with volumes $33 \times 33 \times 14$ mm^3 (Stator I) and $40 \times 40 \times 10$ mm^3 (Stator II) are considered in this study. The considered PM ring dimensions are equal to the ones used in the built experimental bearing prototypes.

4.1 Optimization methodology

Optimizations were performed for the geometries with 6 HTS bulks on the bottom of the stator. This is done to reduce the amount of numerical processing, being expected that the results for geometries with more bulks would be similar. Also, the optimizations were performed with no vertical deviation of the rotor. Several axial deviations were performed for each genetic code (geometry solution) to find the maximum guiding force. Because of the existing symmetry, only $3/16$ of the complete geometry was simulated to reduce the amount of numerical processing. Figures 10(a) and 10(b) show the 3D perspective respectively of the geometry and its simulated partition for the case with 6 bulks of volume $33 \times 33 \times 14$ mm^3 at the bottom of Stator I.

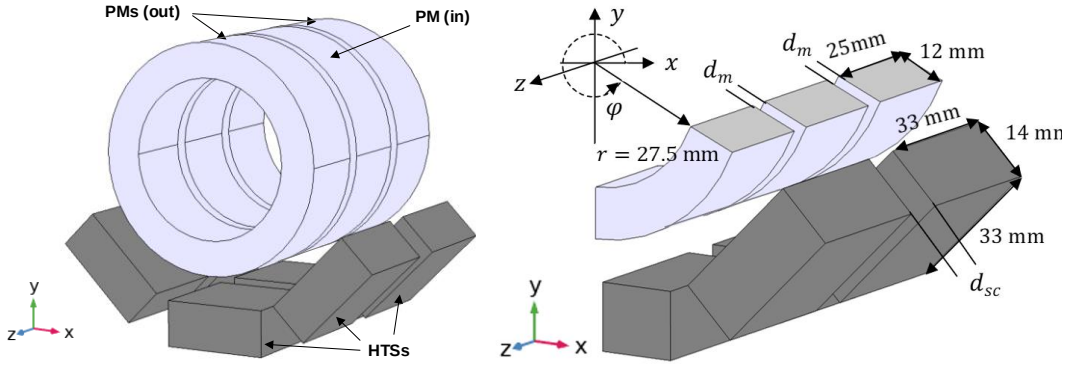

Figure 10: A 3D perspective of the (a) geometry and (b) its simulated partition for the case of Stator I. Figures 11(a) and 11(b) the same for the case with 6 bulks of volume $40 \times 40 \times 10$ mm^3 at the bottom of Stator II.

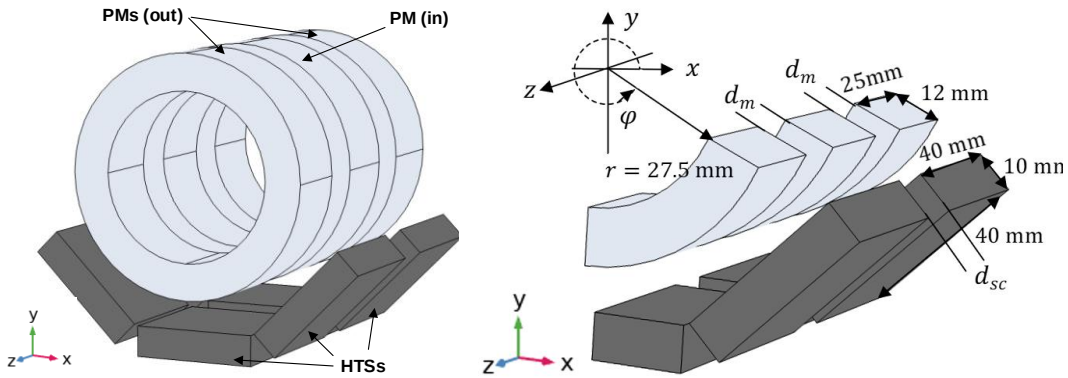

Figure 11: 3D perspective of the (a) geometry and (b) its simulated partition for the case of Stator II.

Optimizations were performed using the equivalent permeability model and not the *E-J* model to significantly reduce the numerical processing time required in the 3D FEA. With better thermal insulation conditions than the ones of the existing experimental prototypes, levitation forces would be closer to the ones predicted using the E-J model with $J_{c0} = 8 \times 10^7$ Am^{-2}. According to Table I resuming the levitation force values with the rotor axis at the center position, the values predicted with $\overline{\mu_r} = 0.25$ are close to the ones predicted with $J_{c0} = 8 \times 10^7$ Am^{-2}. For these reasons, 3D FEA optimization simulations run with $\overline{\mu_r} = 0.25$.

The optimizations in this study were also performed running the NSGA-II over 3D FEA results with $\overline{\mu_r} = 0.25$. As decision variables, it was chosen the distance d_{sc} between the rings of HTS bulks in the stator and the distance d_m between the PM rings in the rotor. The optimizations run with a population size of 150 and for 50 generations. To find the maximum guiding force and corresponding axial deviation, 10 simulations are performed with different axial deviations of the rotor for each genetic geometry.

4.2 Optimization results

Figures 12 shows the Pareto's fronts obtained for the case with 6 bulks of volume $33 \times 33 \times 14$ mm^3 at the bottom of Stator I.

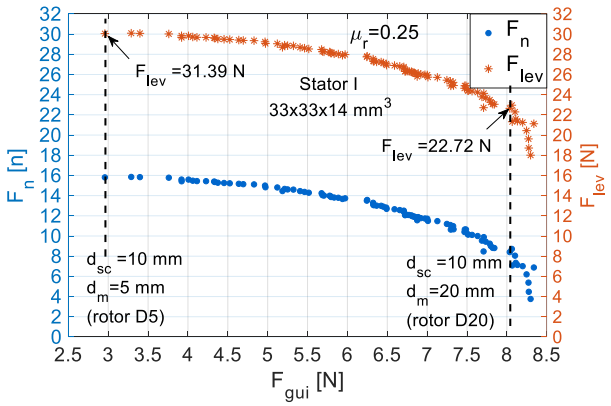

Figure 12: Pareto's front for the case of 6 HTS bulks at the bottom of Stator I.

As expected, the maximum levitation force is verified for the genetic code with $d_m = 5$ mm (rotor D5) and $d_{sc} = 10$ mm, corresponding to one of the two geometries with the levitation and guidance force characteristics presented in section 3. The two vertical dashed lines correspond to the two geometries presented in section 3.

Figure 13 shows the Pareto's front obtained for the case with 6 bulks of volume $40 \times 40 \times 10$ mm^3 at the bottom of Stator II.

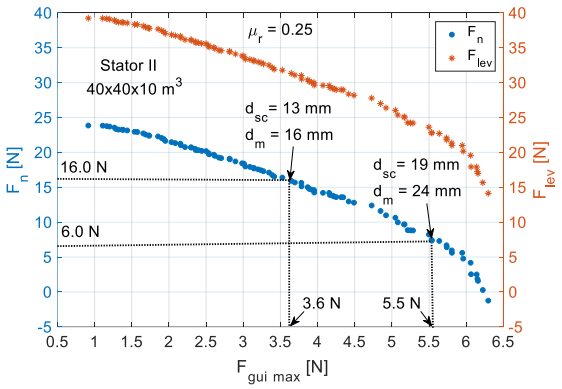

Figure 13: Pareto's front for the case of 6 HTS bulks at the bottom of Stator II.

The geometry with bulks of volume $40 \times 40 \times 10$ mm^3, with $d_m = 16$ mm and $d_{sc} = 13$ mm, guarantees the same minimum levitation force as the geometry with bulks of volume $33 \times 33 \times 14$ mm^3, with $d_m = 5$ mm and $d_{sc} = 10$ mm for which the levitation and guidance force characteristics were presented in section 3. Figure 14 shows the distribution of magnetic flux and current densities obtained by 3D FEA using *E-J* model with $J_{c0} = 8 \times 10^7$ Am^{-2}, for such geometry presenting guiding stability.

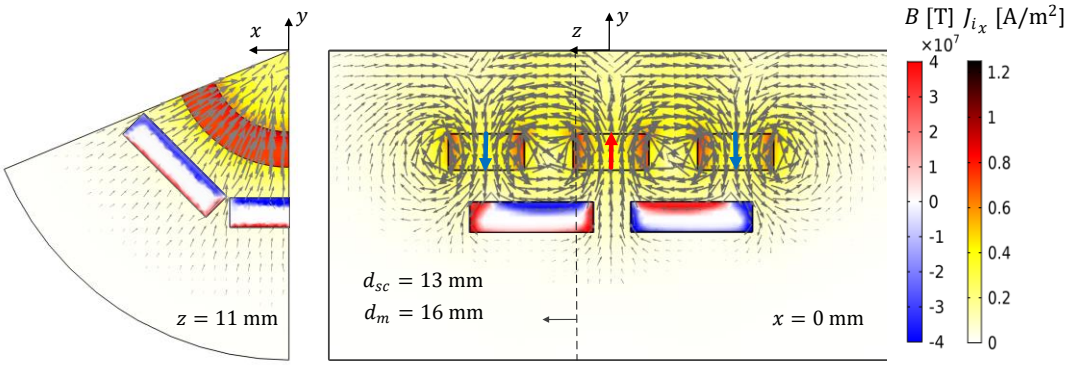

Figure 14: (a) Transversal and (b) longitudinal views with the distributions of **B** and **J** for the geometry with bulks of volume $40 \times 40 \times 10$ mm^3, $d_m = 16$ mm and $d_{sc} = 13$ mm.

With this geometry, the maximum guidance force is $F_{gui\,max} = 3.6$ N while for the geometry with bulks of volume $33 \times 33 \times 14$ mm^3, $d_m = 5$ mm and $d_{sc} = 10$ mm, the maximum guidance force was $F_{gui\,max} = 3.1$ N.

To validate optimization results with Stator II, several experimental measurements for several combinations of distances d_m and d_{sc} were performed with this stator. Plastic bars of 3 mm thick were inserted between the two rings of HTS bulks in Stator II to control d_{sc}. Plastic washers of 2.5 mm thick were inserted between the PM rings to control d_m.

Experimental measurements were performed for the case with $d_m = 17.5$ mm and $d_{sc} = 13$ mm. In this case, five washers of 2.5 mm thick were inserted between the PM rings in addition to the original 5 mm disks of Rotor D5, as shown in Figure 15(a). One plastic bar of 3 mm thick was inserted between the two chambers of Stator II, in addition to their minimum distance of 10 mm, as shown in Figure 15(b). Figure 15(c) shows the measurement of F_n and F_{lev} with no vertical deviation of the rotor from the central position. Figure 15(d) shows the measurement of $F_{gui\,max}$.

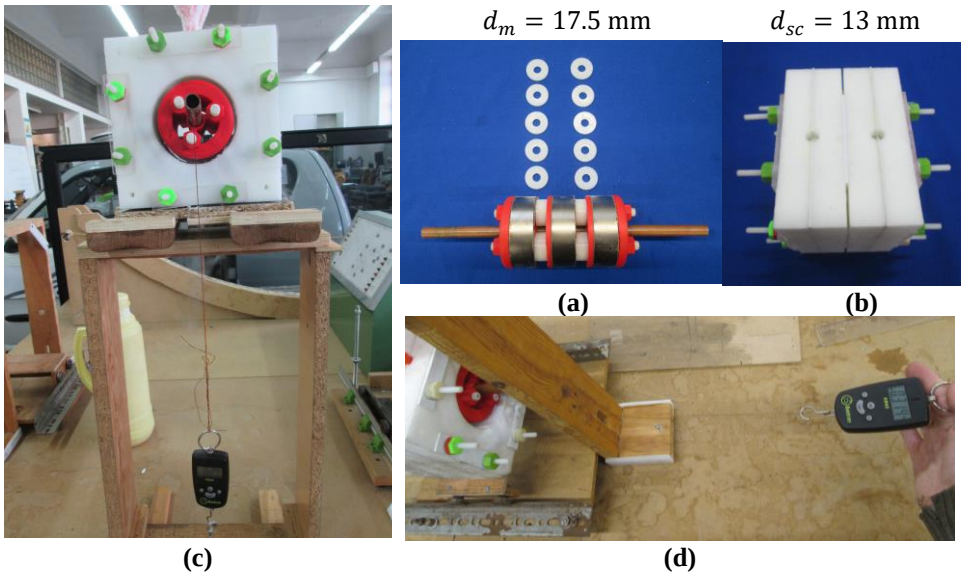

Figure 15: (a) Rotor for $d_m = 17.5$ mm, (b) Stator II for $d_{sc} = 13$ mm, (c) measurement of F_n and F_{lev} with no vertical deviation of the rotor, and (d) measurement of $F_{gui\,max}$.

Figures 16(a) and 16(b) show the F_{lev} and F_{gui} characteristics obtained by 3D FEA with $\overline{\mu_r} = 0.25$ and $J_{c0} = 8 \times 10^7$ Am^{-2}, plotting the experimental measurements of F_{lev} with $\Delta_y = 0$ and of $F_{gui\,max}$. This for the combinations with $d_{sc} = 13$ mm, and $d_m = 15$ mm or $d_m = 17.5$ mm.

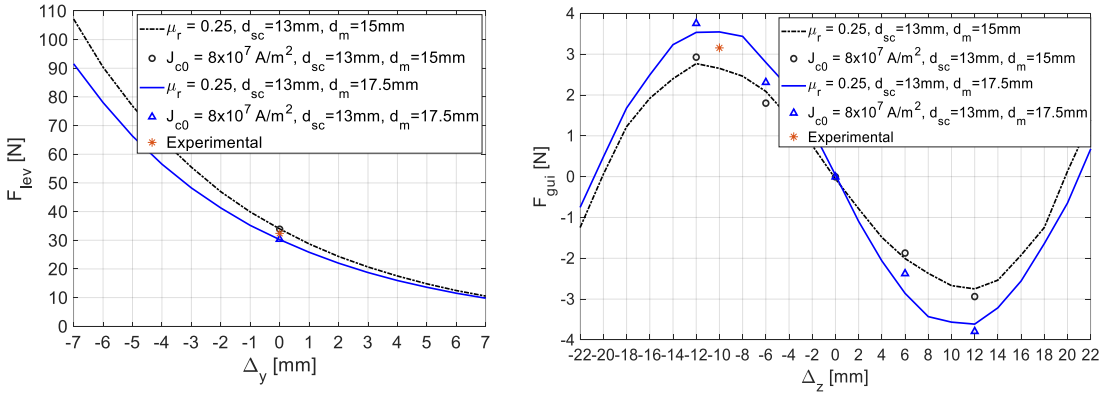

Figure 16: 3D FEA and experimental results for (a) F_{lev}, and (b) F_{gui} with $d_{sc} = 13$ mm, and $d_m = 15$ mm or $d_m = 17.5$ mm.

The geometry with bulks of volume $40 \times 40 \times 10$ mm^3, with $d_m = 24$ mm and $d_{sc} = 19$ mm, guarantees the same minimum levitation force as the geometry with bulks of volume $33 \times 33 \times 14$ mm^3, $d_m = 20$ mm and $d_{sc} = 10$ mm for which levitation and guidance force characteristics were presented in section 3. Figure 17 shows the distribution of magnetic flux and current densities obtained by 3D FEA using *E-J* model with $J_{c0} = 8 \times 10^7$ Am^{-2}, for such geometry presenting guiding stability.

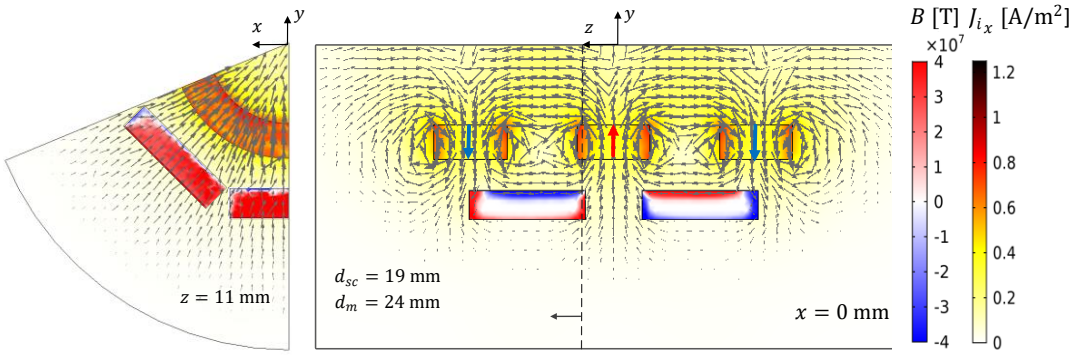

Figure 17: (a) Transversal and (b) longitudinal views with the distributions of **B** and **J** for the geometry with bulks of volume $40 \times 40 \times 10$ mm^3, $d_m = 24$ mm and $d_{sc} = 19$ mm.

With this geometry, the maximum guidance force is $F_{gui\,max} = 5.5$ N while for the geometry with bulks of volume $33 \times 33 \times 14$ mm^3, $d_m = 20$ mm and $d_{sc} = 10$ mm, the maximum guidance force was $F_{gui\,max} = 7.24$ N.

Experimental measurements were performed with $d_m = 25$ mm and $d_{sc} = 19$ mm. In this case, *two* washers of 2.5 mm thick were inserted between the PM rings in addition to the original 20 mm disks of Rotor D20, as shown in Figure 18(a). Three plastic bars of 3 mm thick were inserted between the two chambers of Stator II, in addition to the minimum distance of 10 mm, as in Figure 18(b).

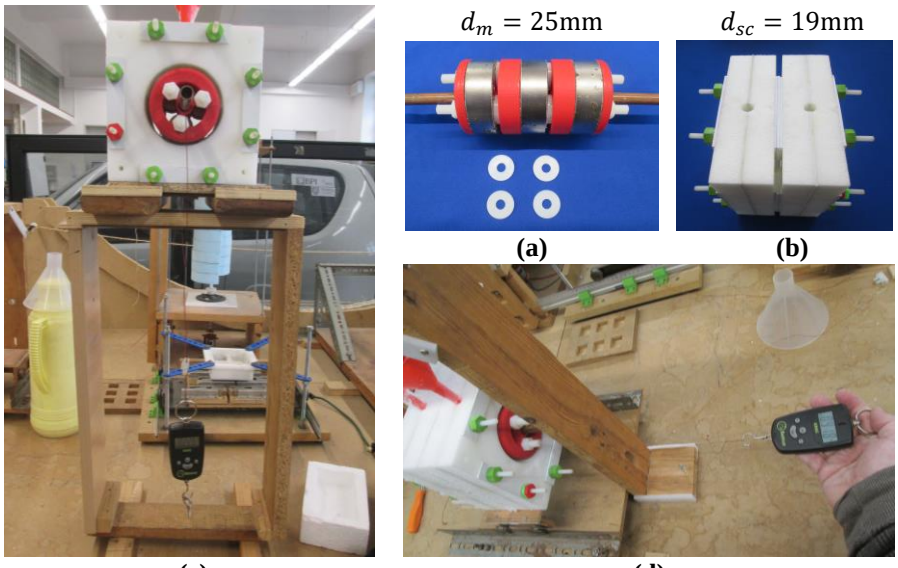

Figure 18: (a) Rotor for $d_m = 25$ mm, (b) Stator II for $d_{sc} = 19$ mm, (c) measurement of F_n and F_{lev} with no vertical deviation of the rotor, and (d) measurement of $F_{gui\,max}$.

Figures 19(a) and 19(b) show the F_{lev} and F_{gui} characteristics obtained by 3D FEA with $\overline{\mu_r} = 0.25$ and $J_{c0} = 8 \times 10^7$ Am^{-2}, plotting the experimental measurements of F_{lev} with $\Delta_y = 0$ and of $F_{gui\,max}$. This for the combinations with $d_{sc} = 19$ mm, and $d_m = 22.5$ mm or $d_m = 25$ mm.

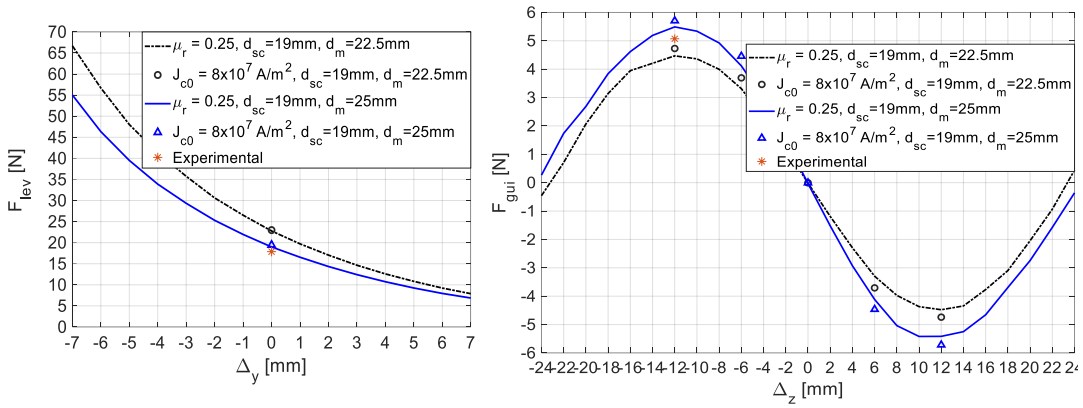

Figure 19: 3D FEA and experimental results for (a) F_{lev}, and (b) F_{gui} with $d_{sc} = 19$ mm, and $d_m = 22.5$ mm or $d_m = 25$ mm.

The value of $F_{gui\,max}$ is higher for the geometry with bulks of volume $33 \times 33 \times 14$ mm^3, spacings $d_m = 20$ mm and $d_{sc} = 10$ mm, than for the geometry with bulks of volume $40 \times 40 \times 10$ mm^3, spacings $d_m = 24$ mm and $d_{sc} = 19$ mm.

5 Identification of guiding stability zones

3D FEA simulations using $\overline{\mu_r} = 0.25$ run for several spacings d_{sc} from 10 mm to 25 mm with steps of 3 mm equal to the thick of the plastic bars inserted between the two rings of HTS bulks in Stator II, and for several spacings d_m from 5 mm to 25 mm with steps of 2.5 mm equal to the thick of the washers inserted between PM rings. Figures 20(a) and 20(b) show the surfaces of F_{lev} respectively for the cases of Stator I and Stator II.

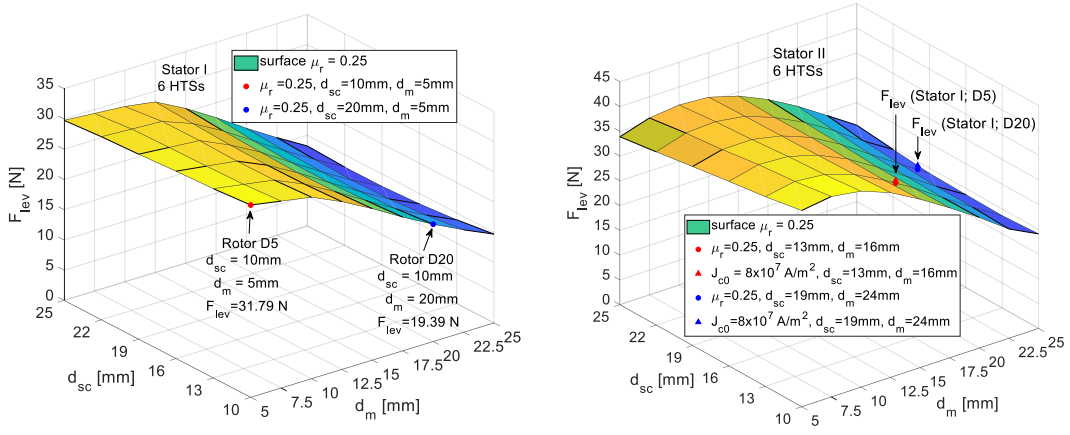

(a) **(b)**

Figure 20: Surfaces of dependence of F_{lev} from d_{sc} and d_m for (a) Stator I, and (b) Stator II.

As one may verify the values of F_{lev} are generally higher for the case of Stator II, including bulks of volume $40 \times 40 \times 10$ mm^3.

Figures 21(a) and 21(b) show the surfaces of $F_{gui\ max}$ respectively for Stator I and Stator II.

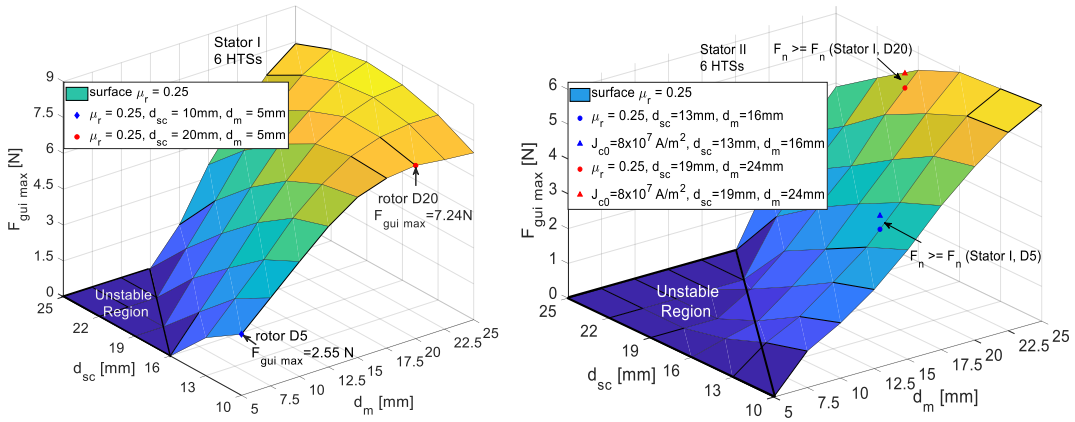

(a) **(b)**

Figure 21: Surfaces of dependence of $F_{gui\ max}$ from d_{sc} and d_m for (a) Stator I, and (b) Stator II.

As one may verify with bulks of volume $33 \times 33 \times 14$ mm^3 (Stator I) the values of $F_{gui\ max}$ are generally higher than with bulks of volume $40 \times 40 \times 10$ mm^3 (Stator II). The region of no guiding stability is also wider for the last case (Stator II).

Figure 22 shows the distribution of magnetic flux and current densities obtained by 3D FEA using E-J model with $J_{c0} = 8 \times 10^7$ Am^{-2}, for one geometry on the limit of the region of no guiding stability with $d_{sc} = 19$ mm and $d_m = 10$ mm.

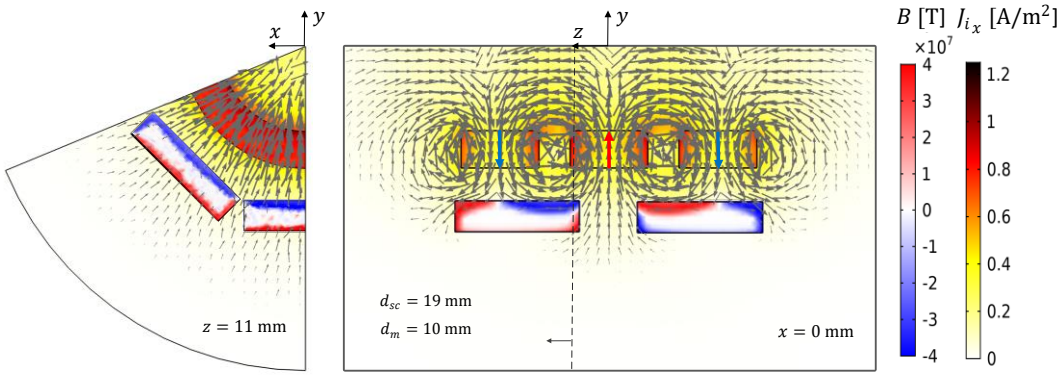

Figure 22: (a) Transversal and (b) longitudinal views with the distributions of **B** and **J** for the geometry with bulks of volume $40 \times 40 \times 10$ mm^3, $d_m = 10$ mm and $d_{sc} = 19$ mm.

As one may verify for this geometry, the bulk extremities are almost coincident with the extremities of the two side PM rings. This generally happens for the geometries on the limit line of guiding stability. Thus, the condition that should be considered for an initial check of the existence of guiding stability is the one expressed by (7)

$$\frac{d_{sc}}{2} + w_{sc} \leq d_m + 3\frac{w_m}{2} \tag{7}$$

from which may be deduced the minimum limit for d_m given by (8)

$$d_m \geq \frac{d_{sc}}{2} - 3\frac{w_m}{2} + w_{sc} \tag{8}$$

Table II presents minimum values of d_m for several values of d_{sc}, on the cases of Stator I and Stator II, calculated using (8).

Table II: Minimum values of d_m (8) for several values of d_{sc}, on the cases of Stator I and Stator II.

	Minimum d_m [mm]	
d_{sc} [mm]	Stator I	Stator II
10	0.5	7.5
13	2	9
16	3.5	10.5
19	5	12
22	6.5	13.5
25	8	15

The values in Table II follow with good approximation the lines on the limit of the guiding stability regions on Figures 21(a) and 21(b).

6 Conclusion

This study aims to present methodologies to determine geometries that maximize the guiding stability of a horizontal axis radial levitation bearing with HTS bulks cooled by ZFC. The guiding stability on the cases of two possible Stators with two different bulk sizes ($33 \times 33 \times 14$ mm^{3}and $40 \times 40 \times 10$ mm^3) for bearing experimental prototypes was studied. The regions of combinations of spacings where there is guiding stability were determined for the two Stator cases. An expression that may be used to identify the limit of the stability region was identified at first sight. The region of combinations of the spacing d_{sc} between the two HTS bulk rings and spacing d_m between PM rings, for which the guiding stability is lower for the case of $40 \times 40 \times 10$ mm^3 size bulks in Stator II than for the case of $33 \times 33 \times 14$ mm^3 size bulks in Stator I. The maximum guiding force $F_{gui\,max}$ for each combination of spacings is generally also higher on the second case. The optimization of spacings performed for the two Stator cases resulted in Pareto's curves from where one can obtain the maximum possible value of $F_{gui\,max}$, for a given restriction on the minimum levitation force F_{lev} that should be guaranteed.

References

Arsénio, A. J., Carvalho, M. V., Cardeira, C., Branco, P.J. C., and Melício, R. (2016) Conception of a YBCO superconducting ZFC-magnetic bearing virtual prototype. IEEE International Power Electronics and Motion Control Conference (PEMC), 25-28 September 2016.

Arsénio, A. J., Roque, M., Cardeira, C., Branco, P. J. C., and Melicio, R. (2018). Prototype of a Zero-Field-Cooled YBCO Bearing with Continuous Ring Permanent Magnets. IEEE Transactions on Applied Superconductivity, 28(4).

Fernandes, J. F. P., Costa, A.J. Arsénio and Arnaud, J. (2020). Optimization of a Horizontal Axis HTS ZFC Levitation Bearing Using Genetic Decision Algorithms Over Finite Element Results. IEEE Transactions on Applied Superconductivity, 30(2).

Quéval, L., Sotelo, G. G., Kharmiz, Y., Dias, D. H. N., Sass F., Zermeño, V. M. R. and Gottkehaskamp, R. (2016). Optimization of the Superconducting Linear Magnetic Bearing of a Maglev Vehicle. IEEE Transactions on Applied Superconductivity, 26(3).

Arsénio, A.J., Melicio, R., Cardeira, C., and Branco, P.J. Costa (2018). The Critic Liquid-gas Phase Transition between Liquid Nitrogen and YBCO HTS bulks: from FEM Modeling to Its Experimental Study for ZFC Levitation Devices. IEEE Transactions on Applied Superconductivity, 28(4).

Arsénio, Antonio J. Costa, and Branco, Paulo J. Costa (2021). Thermo-Hydraulic Analysis of a Horizontal HTS ZFC Levitating Bearing Concerning Its Autonomy Safety Service Time. IEEE Transactions on applied superconductivity 31, (5).

Hong, Z., Campbell, H. M. and Coombs T.A. (2007). Computer Modeling of Magnetisation in High Temperature Superconductors. IEEE Transactions on applied superconductivity, 17(2), (pp. 3761-3764).

Zhang M., and Coombs T.A. (2012). 3D modeling of high-Tc superconductors by finite element software. Superconductor Science and Technology, vol. 25.

Koo, J. H. and Cho G. (2004). Magnetic field dependence on transition temperature Tc in cuprate superconductors. Solid State Communications, 129, (pp. 191-193).

Yamamoto, K., Mazaki, H. and Yasuoka, H. (1993). Magnetization of type-II superconductors in the Kim-Anderson model. Physical Review B, 47(2).

Fujishiro, H., and Naito, T. (2010). Simulation of temperature and magnetic field distribution in superconducting bulk during pulsed field magnetization. Superconductor Science and Technology, 23, 105021.

Peixoto, Inês S. P., Ferreira da Silva, F., Fernandes, João F. P., and Branco, P. J. da Costa (2021). 3D Equivalent Space-Varying Permeability Model of HTS Bulks for Computation of Electromagnetic Forces. IEEE Transactions on applied superconductivity 31, (5).